nature COMMUNICATIONS

ARTICLE

Received 6 Apr 2013 | Accepted 4 Oct 2013 | Published 6 Nov 2013

DOI: 10.1038/ncomms3714

Heterointerface engineered electronic and magnetic phases of $NdNiO_3$ thin films

Jian Liu[1,2,3], Mehdi Kargarian[4], Mikhail Kareev[1], Ben Gray[1], Phil J. Ryan[5], Alejandro Cruz[2], Nadeem Tahir[2], Yi-De Chuang[2], Jinghua Guo[2], James M. Rondinelli[6], John W. Freeland[5], Gregory A. Fiete[4] & Jak Chakhalian[1]

Mott physics is characterized by an interaction-driven metal-to-insulator transition in a partially filled band. In the resulting insulating state, antiferromagnetic orders of the local moments typically develop, but in rare situations no long-range magnetic order appears, even at zero temperature, rendering the system a quantum spin liquid. A fundamental and technologically critical question is whether one can tune the underlying energetic landscape to control both metal-to-insulator and Néel transitions, and even stabilize latent metastable phases, ideally on a platform suitable for applications. Here we demonstrate how to achieve this in ultrathin films of $NdNiO_3$ with various degrees of lattice mismatch, and report on the quantum critical behaviours not reported in the bulk by transport measurements and resonant X-ray spectroscopy/scattering. In particular, on the decay of the antiferromagnetic Mott insulating state into a non-Fermi liquid, we find evidence of a quantum metal-to-insulator transition that spans a non-magnetic insulating phase.

[1] Department of Physics, University of Arkansas, Fayetteville, Arkansas 72701, USA. [2] Advanced Light Source, Lawrence Berkeley National Laboratory, Berkeley, California 94720, USA. [3] Materials Science Division, Lawrence Berkeley National Laboratory, Berkeley, California 94720, USA. [4] Department of Physics, The University of Texas at Austin, Austin, Texas 78712, USA. [5] Advanced Photon Source, Argonne National Laboratory, Argonne, Illinois 60439, USA. [6] Department of Materials Science and Engineering, Drexel University, Philadelphia, Pennsylvania 19104, USA. Correspondence and requests for materials should be addressed to J.L. (email: jian.liu@berkeley.edu).

In Mott insulating oxides, intriguing charge, spin and/or orbital orderings are often found in the presence of localized carriers, for example, in manganites, whereas mobile carriers may experience strong quantum fluctuations resulting in non-Fermi liquid (NFL) behaviour, such as the 'strange metal regime' (a linear T resistivity) in the cuprates[1]. Despite this diversity, the driving interactions in these materials are derived from three essential parameters[2]: the on-site electron–electron repulsion U, the energy difference Δ from the empty local d orbitals to the band-like oxygen p states and their hybridization strength, which is encapsulated in the bandwidth, W. With recent advances in the atomic layering of correlated oxides[3,4], a new route has been established for manipulating the low-energy electronic structure at the nanoscale. Although the quantum criticality of the metal-to-insulator transition (MIT) and the associated magnetic transition has been a key issue in correlated electron systems for decades, it has not been investigated under the versatile controls of oxide heteroepitaxy because of many formidable challenges, especially on probing antiferromagnetic (AFM) orders in ultrathin layers. Leveraging this experimental approach with theoretical advances, however, could bring us closer to ultimately establishing general 'design' rules for engineering desired phases in complex oxide heterostructures (Fig. 1a).

The charge-transfer nickelate family $RENiO_3$ (RE = rare earth) has been one of the fascinating systems for designing innovative oxide interface and heterostructures in last few years[3]. In the bulk, RE = Nd…Lu (except for La) are paramagnetic metals at high temperatures, but become insulating with charge ordering and AFM ordering at T_{MI} and T_N, respectively[5,6]. Within the Sawatzky–Allen–Zaanen scheme, $RENiO_3$ belongs to the class of charge-transfer-type materials where the charge gap corresponds to the excitation of an oxygen $2p$-electron into the unoccupied upper nickel d band[2,7,8] as shown in Fig. 1c. Interestingly, the unusual high 3+ oxidation state of Ni and the presence of a small excitation energy ($\Delta \lesssim 1$ eV), as schematically illustrated in Fig. 1d naturally facilitates the transfer of oxygen p electrons into the unoccupied nickel d-electron states (or alternatively a transfer of a correlated hole onto oxygen)[9]. This 'self-doping' phenomenon results from the coupling of a band-like continuum of oxygen-derived states and localized correlated d states, and is believed to be responsible for the unusual AFM spin ordering ($E'-$type)[5,6,10–13], sometimes described as an '$\uparrow-\uparrow-\downarrow-\downarrow$' stacking sequence of ferromagnetically (FM) ordered planes along the pseudocubic (111) direction, which is characterized by the magnetic vector k = (1/4,1/4,1/4) in cubic notation (see Fig. 1b).

Here we perform a detailed study on ultrathin ~5.7 nm (15 unit cells) films of fully strained $NdNiO_3$ (oriented along the pseudocubic [001] direction) synthesized in a layer-by-layer growth fashion as described in ref. 14. A series of high-quality perovskite-based single-crystal substrates is used to extract the intrinsic dependence on the lattice mismatch ε in a wide range

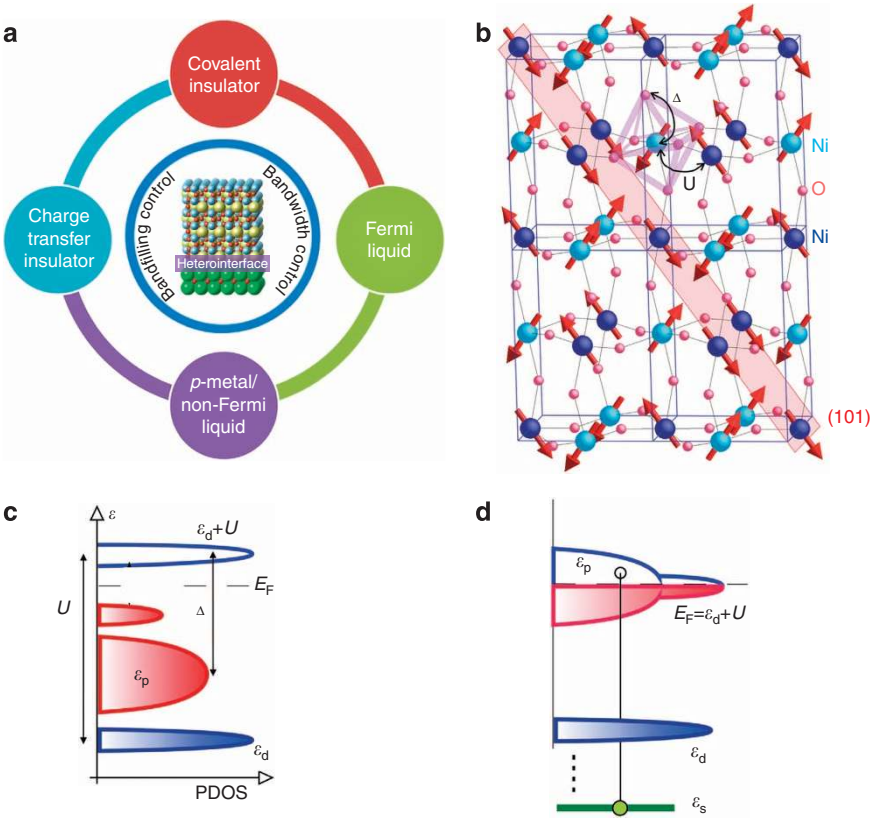

Figure 1 | Charge-transfer correlated oxide. (**a**) Accessibility of latent phases in the heterointerface system. Interfacial constraints control both the band filling through a 'self-doping' effect and the bandwidth allowing new phases to appear that are not observed in bulk systems, even under significant pressure and chemical doping. Phases that may be obtained include a charge-transfer insulator, covalent insulator, p metal, NFL and Fermi liquid. In this work, we report an emergent PI regime and a remarkably stable NFL over a significant portion of the phase diagram. (**b**) Four $NdNiO_3$ orthorhombic unit cells. Arrows denote spins in the associated E'-type AFM structure with the $\uparrow-\uparrow-\downarrow-\downarrow$ stacking of the pseudocubic (111) FM planes, one of which is highlighted in red. One of the octahedra is highlighted to denote the binding with the oxygen ligand holes. (**c**,**d**) Schematics of partial density of states (PDOS) for charge-transfer Mott materials with d- and p-type electrons. Δ is the charge-transfer energy, and U is the on-site d-electron Coulomb repulsion energy. The core-level and $1s \rightarrow 2p$ transition involved in the O K-edge X-ray absorption are indicated in **d**.

from −2.9 to +4% (Table 1). The results reveal full control of epitaxy on the MIT and the magnetic ordering. Specifically, tuning the amount of epitaxial strain from the tensile to compressive side first merges the MIT and AFM transition, followed by a rapid decay of the magnetic ordering into a spin-disordered phase (possible quantum spin liquid (SL)) before stabilizing a conducting NFL phase. In this work, we show that the underlying electronic reconstruction is associated with simultaneous modulation of the bandwidth, W, and the self-doping, determined by Δ.

Results

Phase diagram. To determine the evolution of the electronic and magnetic states, we employed temperature-dependent measurements of both resistivity and resonant X-ray diffraction of the magnetic ordering peak. Figure 2a summarizes the lattice mismatch-temperature phase space. As seen, despite the ultrathin form and the large lattice mismatch on some of the substrates, the metallicity is well preserved for all samples at room temperature. A direct inspection of the temperature-dependent resistivity curves from 5 to 300 K for different lattice mismatch, ε in Fig. 2b indicates the presence of well-controlled and diverse electronic phase behaviours in the ultrathin films that are absent in bulk $NdNiO_3$. Specifically, for samples in the positive ε range (under tensile strain), the insulating ground state continuously develops with increasing magnitude of ε, whereas an unusual metallic NFL phase emerges and persists throughout the whole range of negative ε (compressive strain). The absence of the bulk-like first-order MIT near $\varepsilon \approx 0$ manifests the unique role of the hetero-epitaxy in destabilization of Mott insulating state with charge and spin orderings; because of the interface-imposed lattice boundary condition, collective long-range order that strongly couples to the lattice degrees of freedom may be frustrated. In addition, even for $\varepsilon = 0$, a substrate can still strongly distort the film structure via internal structural mismatches such as octahedral rotation,

Table 1 | In-plane pseudo-cubic lattice constants, a_{sub}, of the used substrates[57,58] and their corresponding lattice mismatch (ε) with $NdNiO_3$ (3.803 Å).

	$YAlO_3$	$SrLaAlO_4$	$LaAlO_3$	$SrPrGaO_4$	$SrLaGaO_4$	$NdGaO_3$	$(La_{0.3}Sr_{0.7})(Al_{0.65}Ta_{0.35})O_3$	$SrTiO_3$	$DyScO_3$
a_{sub} (Å)	3.692	3.757	3.794	3.812	3.843	3.858	3.868	3.905	3.955
ε (%)	−2.9	−1.2	−0.3	0.3	1.1	1.4	1.8	2.7	4.0

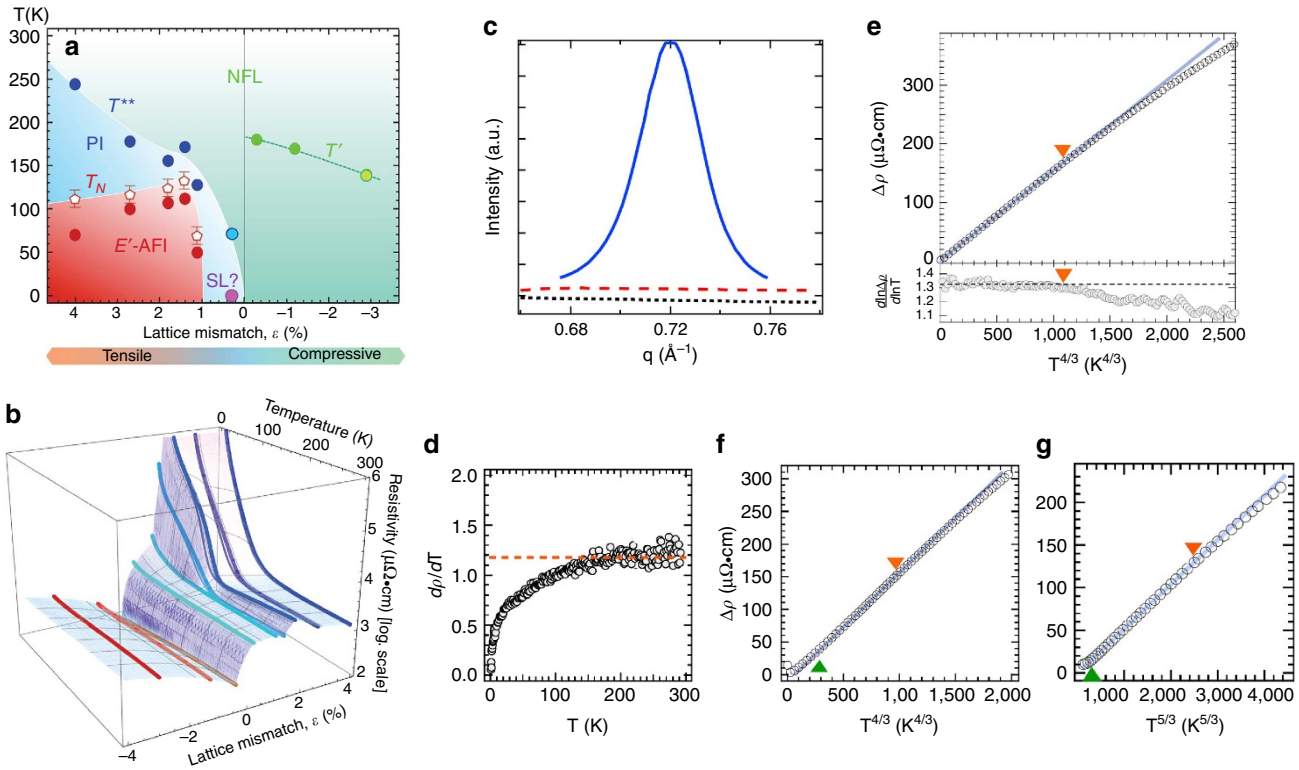

Figure 2 | Phase evolution with heteroepitaxial constraint. (**a**) Lattice mismatch-temperature phase diagram. NFL, PI and AFI denote non-Fermi liquid, paramagnetic insulator and AFM insulator, respectively. T^{**} (blue), T' (green) and the hysteric inflection point (red) are denoted by close circles, whereas T_N is denoted by open pentagon and its error bar is defined as the temperature step size, 10 K. (**b**) Temperature-dependent resistivity versus heteroepitaxial lattice mismatch. (**c**) q-scans across the E'-type AFM reflection intensity at k = (1/4,1/4,1/4) ((1/2,0,1/2) in orthorhombic notation) observed by resonant X-ray diffraction at the Ni L_3-edge at 12 K (blue solid line at $\varepsilon = +1.8\%$ and dashed black line at $\varepsilon = +0.3\%$) and 140 K (red dashed line at $\varepsilon = +1.8\%$). (**d**) the temperature derivative of the resistivity, indicating a T-linear behaviour at high temperatures at $\varepsilon = -0.3\%$. Fit-free analysis of the $T^{4/3}$ power-law behaviour for $\varepsilon = -0.3\%$ (**e**) and -1.2% (**f**), and the $T^{5/3}$ power-law behaviour for $\varepsilon = -2.9\%$ (**g**). The upper red triangle signals the upper temperature limit T' where the resistivity crosses over to a linear T behaviour. The lower green triangle indicates the lower temperature where the temperature dependence starts to deviate.

distortion and crystal symmetry. Meanwhile, the strain-induced MIT signals that the heteroepitaxial $NdNiO_3$ is in close proximity to quantum criticality near $\varepsilon \approx 0$. Although the discrete values of ε limit the ability to precisely pinpoint the location of the critical end point of the 'E-AFI' region, magnetism is rapidly suppressed on the insulating side on approach to $\varepsilon \approx 0$ and appears to join the low-temperature NFL region for $\varepsilon < 0$ by an intervening ground state without long-range magnetic ordering (a possible quantum SL) as shown in Fig. 2a.

On the insulating side ($\varepsilon > 0$), Fig. 2a shows the evolution of characteristic transition temperatures, that is, T^{**} (resistivity minimum temperature) for marking the emergence of the insulating phase, and T_N for depicting the onset temperature of the magnetic ordering peak of the low-temperature E'-AFI phase. In particular, for large values of ε, the T^{**} is significantly higher than T_N. This behaviour is sharply distinct from bulk $NdNiO_3$ where $T^{**}(=T_{MI})$ coincides with T_N. The resulting intermediate temperature paramagnetic insulating (PI) phase thus implies the opening of a gap, which is decoupled from the spin ordering. It is important to note that this PI phase is unattainable in bulk $NdNiO_3$—an example of a latent electronic phase in this system stabilized by the heterointerface. As ε is reduced, T^{**} and T_N merge albeit with a different slope, that is, while T^{**} quickly decreases, T_N steadily rises until $\varepsilon \approx +1.8\%$. This convergence of critical temperatures is further evidenced in the enhanced thermal hysteresis of the resistivity around $\varepsilon \approx +1.8\%$ (see Figs 2b and 5b). It can be seen in Fig. 2a that the hysteresis centre, estimated as the hysteric inflection (Fig. 5a), also follows an ε dependence similar to T_N, although the onset temperatures of the magnetic reflection are somewhat higher because of the two-phase coexistence within the finite width of the hysteresis.

As shown in Fig. 2a, for $\varepsilon \lesssim +1.8\%$, the evolution of T_N qualitatively changes so that T_N and T^{**} exhibit approximately a 'parallel dive' in response to reducing ε. On further lowering ε towards zero, T_N rapidly vanishes accompanied by a drastically weakened thermal hysteresis in resistivity (see Figs 2b and 5b), for example, at $\varepsilon \approx +1.1\%$. The thermal hysteresis completely recedes from the system at around $\varepsilon \approx +0.3\%$ (Fig. 4). The inset of Fig. 2c shows that no E'-type AFM reflection is observed at $\varepsilon = +0.3\%$ down to 12 K, in contrast to that at $\varepsilon = +1.8\%$, for example. On the other hand, T^{**} remains finite with the tendency of suppression towards zero. This is distinct from the bulk where increasing hydrostatic pressure maintains the hysteric resistivity while suppressing the insulating state[15]. The insulating nature of the ground state at $\varepsilon = +0.3\%$ is further verified by analysis according to the Möbius criterion[16]. The difference in the behaviour of T^{**} and T_N thus strongly suggests the emergence of an unusual weakly insulating ground state with completely quenched long-range AFM order in the vicinity of $\varepsilon = 0\%$. The stabilization of this emergent spin-disordered state implies enhanced frustration in proximity to the zero temperature MIT, which presents an intriguing candidate for a quantum SL[17,18].

On crossing the zero temperature MIT towards negative values of ε, the temperature-driven MIT is completely quenched and a new exotic metallic ground state emerges across the entire range of $\varepsilon < 0$. To stress the peculiarity of the phase, we point out that at 'high' temperatures but still well below the Debye temperature $\sim$420 K (ref. 19), the resistivity exhibits extended unconventional linear T dependence (see Fig. 2d) commonly seen in the 'strange metal' regime of the high-T_c cuprates[1], whereas Fermi liquids have a T^2 dependence. On crossing the intermediate temperature scale ($\sim$150 K) marked as T' in Fig. 2a, however, another characteristic temperature dependence clearly appears. A fitting-free resistivity data analysis (see Fig. 2e,f) reveals a $T^{4/3}$ power-law behaviour lingering over a 100-K temperature range. The 4/3 power-law behaviour is characteristic of a NFL in the vicinity of a two-dimensional (2D) quantum critical point with dynamical exponent $z = 3$ (ref. 20). For the large negative values of $\varepsilon \lesssim -2.9\%$, the power of the NFL exponent below T' switches to 5/3 with increasing compressive strain (see Fig. 2g). The 5/3 exponent is characteristic of a three-dimensional (3D) critical point with dynamical exponent $z = 3$ (ref. 20). Although we do not detect any sizable structural transition that might cause a change in the effective dimensionality of our system (from 2D to 3D) near $\varepsilon \approx -3\%$, theoretically, large biaxial compression could drive such a transition in $NdNiO_2$ (ref. 21).

The observed NFL features in transport imply the presence of strong quantum fluctuations stabilized by the heteroepitaxial boundary. Indeed, as discussed above, the simultaneous rapid collapse of the AFM order and the emerging spin-disordered phase also highlights the important difference of this new quantum melting regime from that of the bulk where a $T_{MI} = T_N$ phase boundary is driven to a single critical end point. To the best of our knowledge, bulk $NdNiO_3$ does not exhibit the NFL behaviour reported here for $\varepsilon < 0$ under either hydrostatic or chemical pressure[5,6,22], nor have been the 4/3 and 5/3 exponents reported for the $RENiO_3$ series, except the bulk $PrNiO_3$ under high hydrostatic pressure[15]. A comparison with our system, however, reveals that the heterointerface-driven NFL phase is characterized by a markedly higher onset temperature T' (that is, 200 versus 40 K in bulk $PrNiO_3$). Moreover, although the hydrostatic pressure also suppresses the MIT in bulk $PrNiO_3$, it is accompanied by stronger and stronger hysteric behaviour[15] in sharp contrast to the observations here. La-doped $NdNiO_3$ is also reported to show a NFL behaviour but with an exponent equal to 3/2 (ref. 22). This seemingly small difference in the numerical values, however, imply very different underlying critical phenomena giving rise to the fluctuations; a value of 3/2 indicates finite wavevector fluctuations, whereas 4/3 and 5/3 reflect fluctuations at zero wavevector. It is remarkable that the heteroepitaxial constrain is able to not only stabilize the metallic state but also control the underlying dynamics in a thin film form, facilitating potential applications that would not be possible in the bulk.

Note that the NFL exponent is stabilized over such a wide range of temperatures and negative ε in our experiments. Because of the absence of long-range magnetic ordering[23,24], this behaviour is qualitatively and even semiquantitatively consistent with a Boltzmann-type transport theory involving multiple bands of different effective masses and zero-momentum critical fluctuations in the heaviest of the bands[20]. Our density functional theory (DFT) calculations support the multiple band picture of different masses, and the structure of the transport theory provides a natural mechanism for the crossover of a fractional exponent at lower temperatures (4/3 or 5/3) to the linear T behaviour observed above T' but still below the Debye temperature. The precise character of the zero-momentum quantum fluctuations remains unclear at present, and further experimental and theoretical work is due.

ε-dependence of ligand hole and Madelung potential. To elucidate the electronic energy scales involved in controlling these emergent phases (PI, NFL and possible quantum SL), we have performed extensive resonant soft X-ray spectroscopy (XAS) measurements on the oxygen K-edge, which directly probes the hole state in the unoccupied $2p$-projected density of states[25]. By utilizing the $1s \rightarrow 2p$ transition on the oxygen K-edge (see Fig. 1d), that is, $3d^8\underline{L} \rightarrow \underline{1s}3d^8$ ($\underline{L}$ denotes the ligand hole state), we evaluate the connection between the insulating phase behaviour and 'self-doping' behaviour. In addition, due to the previously reported energy shift in oxygen K-edge XAS as a function of chemical

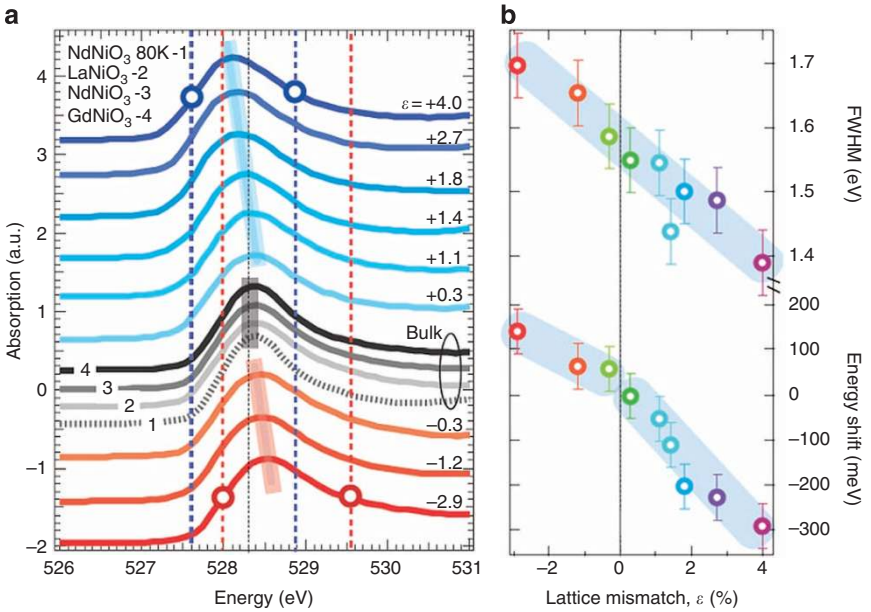

Figure 3 | X-ray absorption spectroscopy. (**a**) Soft X-ray absorption spectra of $NdNiO_3$ ultrathin films at O K-edge at 300 K. Three reference spectra at 300 K and one at 80 K from bulk $LaNiO_3$, $NdNiO_3$ and $GdNiO_3$ are included for comparison. Dashed lines and shaded boxes are guides for eye. The open circles on the top and bottom spectra indicate the FWHM. (**b**) The pre-peak FWHM around 529 eV and the energy shift of the pre-peak versus lattice mismatch ε. Their errors are limited to the photon energy resolution, 0.1 eV. Shaded bars are guides for eye.

pressure in the bulk[26], we have also measured a set of high-quality bulk ceramic samples of $LaNiO_3$, $NdNiO_3$ and $GdNiO_3$ to provide a direct benchmark comparison for resolving the underlying physics of heterointerface control. To obtain precise information on the photon energy, all the spectra were aligned to a standard, which was measured simultaneously with the samples.

Figure 3a shows the resulting X-ray absorption spectra obtained at the threshold energy around 528.5 eV where the absorption pre-peak is exclusively because of Ni 3*d* states hybridized with O 2*p* states[25]. As clearly seen, the pre-peak around 529 eV exhibits a remarkably large and asymmetric (with the sign of ε) energy shift, indicative of an evolution in the charge excitation energy. Figure 3b quantifies the finding as follows: the oxygen-derived band edge moves downwards by as much as 270 meV at $\varepsilon = +4\%$ (or $\sim$80(13) meV/%) and upwards by $\sim$150 meV at $\varepsilon = -2.9\%$ (or $\sim$34(13) meV/%). In sharp contrast to this result, the shift is completely absent for the bulk data (shown as grey shaded curves in Fig. 3a) when varying chemical pressure and/or temperature crossing the MIT into the charge-ordered AFM insulating state. These results point to the pivotal role of the epitaxial substrate lattice mismatch as the driving force for the observed shift. Although the decrease of the absorption threshold is strikingly similar to that seen from the introduction of holes and in-gap states through conventional chemical doping[27], the 'hole-doping' response here is achieved by shifting the entire pre-peak in virtue of heterointerface strain in the absence of explicit chemical doping.

The large observed shift of the excitation energy to the unoccupied states is connected to the shift of the O 1s core-level states with respect to the Ni 3*d*-hybridized state. This manifests itself through an altered relative Madelung site potential between Ni and O, which is the primary effect that defines the magnitude of the charge excitation energy Δ (ref. 28). This finding lends strong support to the notion of a modulation of the fundament energy scale $-\Delta$ with ε (refs 1,29). In addition, the pre-peak width, a measure of a degree of *p*–*d* hybridization or covalency *W*, scales almost linearly with ε (see Fig. 3), in accordance with the induced MIT. Microscopically, the decreasing *W* as a function of ε can be attributed to longer in-plane Ni-O bonds, as strain must be accommodated by changing either the in-plane bond length or bond angle, whereas the later would instead result in an increasing *W*. The combined modulations in both Δ and *W* reflects the unique control of ultrathin $NdNiO_3$ in a 'self-doped' material. In particular, the simultaneous regulation of the self-doped oxygen hole density via both Δ and *W* is expected to tune the balance between the FM and AFM exchange channels of the Ni-O-Ni bond in the *E*′-type spin ordering[10]. Thus, deviation in the degree of self-doping would transpire to cause strong frustration and act to suppress the spin order, especially near the MIT, resulting in the collapse of the AFM ordering and a possible quantum SL state.

Discussion

In summary, we have demonstrated the consequences of heterointerface constraints from substrate lattice mismatch and used it to drive emergent phase behaviour and induce quantum critical behaviour not reported in the bulk series of $RENiO_3$. This control is achieved through the modulation of the covalency, *W*, and charge transfer energy, Δ with ε. We have demonstrated that a specific ground state can be selected by the fine balance of the self-doped hole density on the oxygen atoms. We expect that the physics uncovered for $NdNiO_3$ is rather general and should open the door to the rational design of new classes of correlated electron materials with a wider range of applications through an enriched phase diagram.

Methods

Experimental details. Ultrathin $\sim$5.7 nm (15 unit cells) films of fully strained $NdNiO_3$ are grown along the pseudocubic [001] direction by pulsed laser deposition with *in situ* reflection high-energy electron diffraction. A layer-by-layer growth fashion is controlled by monitoring the reflection high-energy electron diffraction specular intensity[14]. Table 1 shows the in-plane pseudocubic lattice constants, a_{sub}, of the used substrates. The corresponding lattice mismatch (ε) with $NdNiO_3$ (3.803 Å) is derived as $\frac{a_{sub}-3.803}{3.803}$. Resistivity is measured with the van der Pauw method in a physical property measurement system. Resonant magnetic

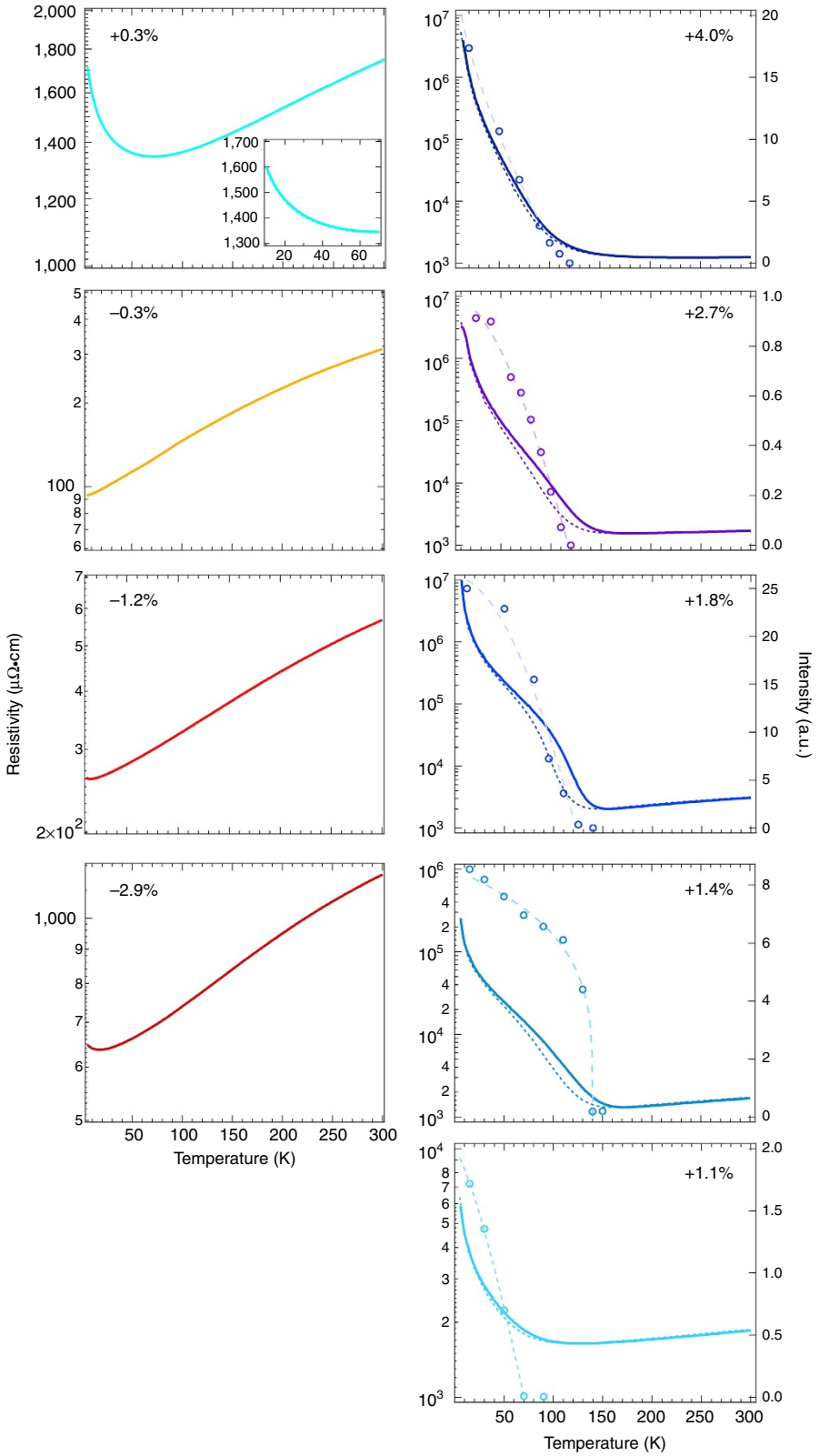

Figure 4 | Temperature-dependent resistivity and resonant X-ray diffraction. Left axis corresponds to resistivity. Cooling resistivity data are shown as dashed curves for samples that have thermal hysteresis. Cooling resistivity data at $\varepsilon = +0.3\%$ are included in the inset to demonstrate the absence of hysteresis. Right axis is for diffraction intensity (open circles) of the k = (1/4,1/4,1/4) reflection for samples where this ordering peak is observed. Dashed lines are used as guides for eyes for the diffraction intensity data.

X-ray diffraction at the Ni L_3-edge is utilized to directly track the E'-type AFM ordering[30]. This measurement is done in the RSXS endstation at beamline 8.0.1 of the advanced light source[31]. The emerging intensity of the magnetic Bragg reflection at the magnetic vector k = (1/4,1/4,1/4) is monitored as a function of temperature, such as that at $\varepsilon = +1.8\%$ shown in Fig. 2c. Data at each temperature are taken after the cryostat temperature control fully settles and the sample

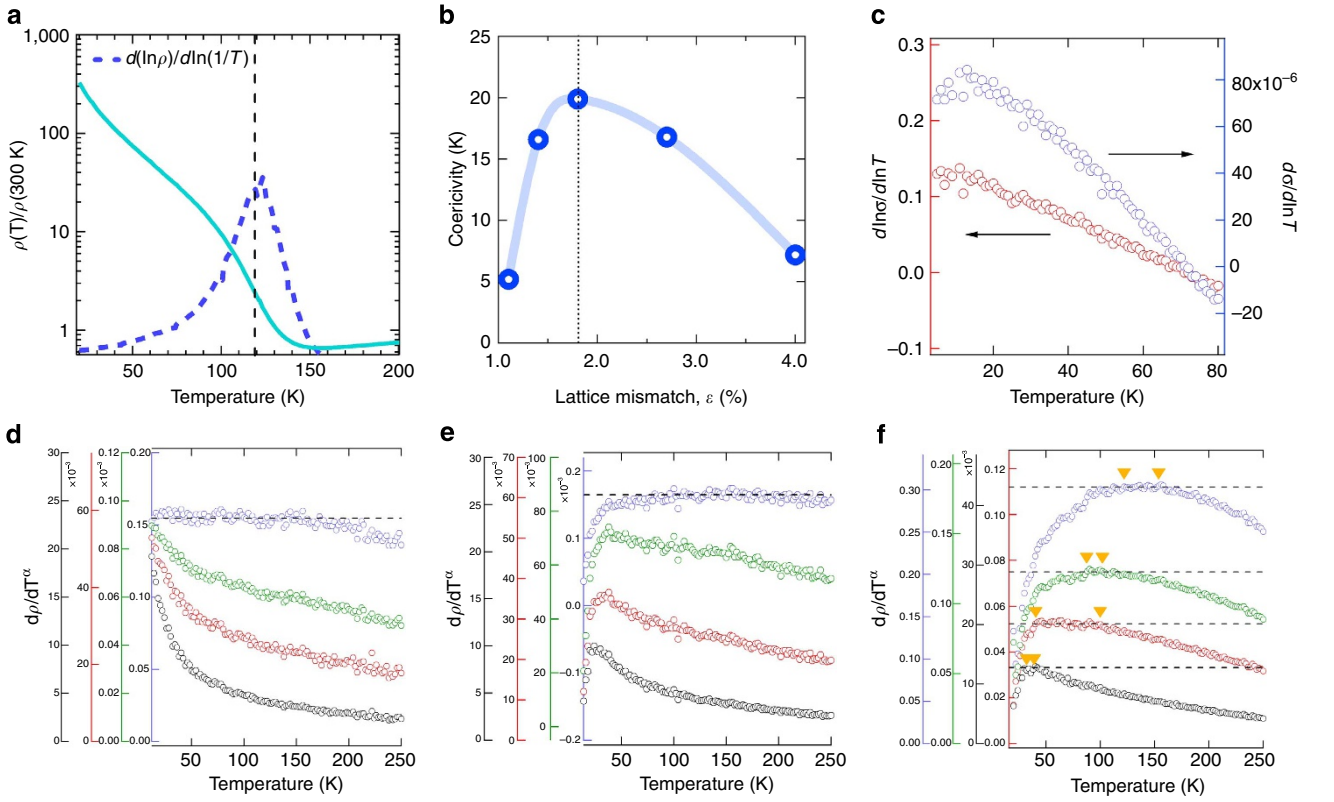

Figure 5 | Resistivity data analysis. (**a**) An example of the resistivity inflection point T_N derived from $(\frac{d\ln\rho}{d(1/T)}\mid_{max})$ on the insulating side of the strain ($\varepsilon>0$). (**b**) The thermal hysteresis coercivity versus strain. (**c**) Conductivity derivatives for $\varepsilon=+0.3\%$ versus temperature. Temperature-dependent resistivity derivatives (open circle) with respect to the temperature power-law function with the power index α equal to, from top to bottom, 4/3 (blue), 3/2 (green), 5/3 (red) and 2 (black) for $\varepsilon=-0.3\%$ (**d**), -1.2% (**e**) and -2.9% (**f**). Dash lines are guides for eyes. For $\varepsilon=-2.9\%$, triangles are used to indicate the temperature region where the derivative may be considered as a constant within the noise.

position/alignment is examined. Oxygen K-edge X-ray absorption spectroscopy is performed at beamline 4-ID-C of the advanced photon source (APS) with an energy resolution of 0.1 eV. The bulk reference samples are prepared through high-pressure synthesis[32] by Professor Bogdan Dabrowski from the Northern Illinois University.

Lattice mismatches. Transport data and resonant X-ray diffraction data are shown in Fig. 4. Bulk $ReNiO_3$ (except Re = La) is paramagnetic metal at high temperatures and becomes insulating and antiferromagnetically ordered at T_{MI} and T_N, respectively. Differential calorimetry scanning indicated that T_{MI} is shifted in all nickelates between heating and cooling up to 10–20 K (refs 33,34). Thermal hysteresis has also been observed in direct current resistivity when T_N is nearby or coincide with T_{MI}, for example, Re = Pr and Nd (ref. 35). As $T_N \ll T_{MI}$, reported resistivity data showed that the hysteretic behaviour is highly suppressed or absent[36–38]. The underlying cause to this difference between the two techniques requires further study in the bulk. Here we deduced the phase behaviour of the $NdNiO_3$ ultrathin films by identifying two important temperatures. The first one is the resistivity minimum temperature T^{**}, which marks the position of $\frac{d\rho}{dT}\mid_{T=T^{**}}=0$ signifying the emergence of a charge excitation gap. The other characteristic temperature scale is deduced from the onset of the magnetic ordering peak denoted as T_N in Fig. 2a. The onset of the magnetic peak is also very close to the onset of the thermal hysteresis of resistivity. The evolution of the transitions controlled by heterointerface constraint is discussed in the main text. From Fig. 4, one can also see that the size of the thermal hysteresis (that is, thermal coercivity) is rapidly decreasing as ε decreases from $+1.8\%$ towards zero, and completely disappears at $\varepsilon=+0.3\%$. The ε dependence of the coercivity is showed in Fig. 5b and consistent with that of T_N. The centre of the hysteresis can be estimated by the hysteric inflection point $(\frac{d\ln\rho}{d(1/T)}\mid_{max})$ in that regime (Fig. 5a) and its ε dependence is also similar to T_N as discussed in the main text. Figure 5c shows that the log–log derivative of the conductivity for $\varepsilon=+0.3\%$ is continuously increasing with lowering temperature, verifying the insulating nature according to the Möbius criterion[16]. The temperature-dependent derivative with respect to ln(T) also rules out the possibility of a 2D disordered metal[39].

Figure 5d–f compare the temperature-dependent resistivity derivatives with respect to the different power-law functions with the power index α equal to 4/3, 3/2, 5/3 and 2 for $\varepsilon=-0.3$, -1.2 and -2.9%. This fit-free analysis further corroborates the power-law assignment and the temperature boundary of the NFL state (see main text). In particular, it can be clearly seen that the 4/3 power-law is the best description for $\varepsilon=-0.3$ and -1.2% as the derivative is weakly temperature-dependent for an extensive region at low temperatures. For $\varepsilon=-2.9\%$, the derivatives with $\alpha=4/3$, 3/2 and 2 may be considered to be weakly temperature dependent within very limited ranges probably due to being close to the tops of the derivative curves. In contrast, the $\alpha=5/3$ derivative is evidently temperature independent in a relatively wide region at low temperatures.

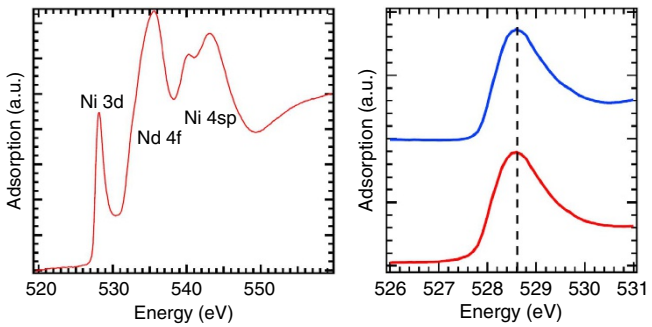

Figure 6 | Oxygen K-edge spectrum. Left: oxygen K-edge X-ray absorption spectrum for $\varepsilon=+2.7\%$ at 300 K. Right: the pre-peak region of the spectra at 300 K (red, bottom) and 10 K (blue, top).

Representative oxygen K-edge X-ray absorption spectrum is shown in a wide energy range in Fig. 6 at $\varepsilon=+2.7\%$. The first peak at about 528 eV corresponds to the Ni 3*d*-hybridized states. The second one at about 535 eV comes from states hybridized with the 4*f* and 5*d* orbitals of Nd and other RE elements if contained in the substrates. The features at 540 eV or above mainly originate from bands

formed with Ni 4*sp* states and other metal ions in the substrates. Figure 6 compares the energy positions of the first peak at 300 and 10 K, demonstrating no energy shift across the temperature-induced phase transitions. Note that, in contrast to the reported bulk data[26], no energy shift was found in our bulk spectra in Fig. 3a. To exclude potential beamline energy drift, all the spectra here were aligned to a standard that was measured simultaneously with the samples. Possible difference may also come from the energy resolution, which is 0.1 eV here and 0.35 eV in ref. 26.

Theoretical model of NFL physics. Compared with bulk $NdNiO_3$, one of the main results to emerge in our study is the presence of new electronic phases in the heterointerfacial structure, namely, the PI regime, and the emergence of an extended NFL regime that appears under compressive strain. As the paramagnetic insulator is featureless (and possibly contains a quantum SL at zero temperature and small ε), we focus here on the physics probably underpinning the NFL behaviour.

The NFL behaviour is observed in electrical transport and is shown in Fig. 2. In a Fermi liquid, phase-space arguments applied to low-energy electron–electron scattering around the Fermi energy leads generically to an electrical resistivity that scales as the second power of the temperature, $\rho(T) \propto T^2$. Resistivity that scales as $\rho(T) \propto T^{\alpha}$ for $\alpha \neq 2$ is considered NFL. As shown in Fig. 2a in the main text, for $\varepsilon < 0$, we find $\alpha \neq 2$. In particular, for $\varepsilon = -0.3$ and -1.2%, $\alpha = 4/3$ for $T < T'$ and $\alpha = 1$ for $T > T'$, whereas for $\varepsilon = -2.9\%$, $\alpha = 5/3$ for $T < T'$, and $\alpha = 1$ for $T > T'$.

The NFL transport exponents imply the presence of degrees of freedom beyond the electrons themselves and are often associated with quantum critical behaviour. Thus, common band structure methods, such as DFT, are not able to entirely capture this physics. Nevertheless, DFT is believed to provide a good approximation in many cases to the underlying single-particle physics that interacts with additional degrees of freedom that may be critical. In the following, we argue that the main features of the NFL physics we report here can be successfully accounted for by a multiband model in the presence of zero-momentum ($\vec{q} = 0$) critical fluctuations.

DFT results. We compute the electronic band structure of tetragonal $NdNiO_3$ using DFT with the projector-augmented wave (PAW) formalism[40] as implemented in the Vienna *Ab initio* Simulation Package[41,42]. We used the Perdew–Burke–Ernzerhof (PBE)-generalized gradient approximation[43] plus Hubbard *U*-method[44] (PBE + *U*). We chose the spherically averaged form of the rotationally invariant effective *U* parameter introduced by Dudarev *et al.*[45] with a $U_{\mathrm{eff}} = 4.0$ eV (hereafter, *U*) on the correlated Ni 3*d* orbitals. Because of self-interaction errors, *f* electrons may be poorly treated by the commonly available exchange-correlation functionals in DFT. One common approach to handle the inabilities of the local spin-density approximation L(S)DA or PBE(sol) functionals in describing the localized *f* electrons is to explicitly place those more localized electrons in the core of the pseudopotential. Here we used the PAW method to represent the ionic cores and followed that procedure. As Nd has a total of 6 valence electrons (four *f* electrons and two *s* electrons) and in $NdNiO_3$, Nd adopts a valence of 3+, three 4*f* electrons are placed (frozen) in the core when the PAW is generated. This PAW is then used in all subsequent calculations. This approach has been reported to give reliable structural and electronic properties for $NdNiO_3$, as reported recently by Prosandeev *et al.*[46]

We impose *A*-type AFM order as an approximation to the complex *E*′-AFM spin configuration found in the bulk equilibrium phase. The Brillouin zone (BZ) is sampled with a minimum of $9 \times 9 \times 9$ *k*-point mesh, and reciprocal space integrations performed with Gaussian smearing of width 5 meV.

The atomic structure is constrained to have *P*4/*mmm* crystallographic symmetry, and we relax the free lattice constants *a* and *c* until the cell stresses are zero. For the analysis here, we omit structural distortions due to both rotations of octahedra and breathing distortions to evaluate the electronic structure and band dispersions in a pseudomorphically grown film. The role of octahedral rotations is known to reduce the electronic bandwidth while also doubling the size of the unit cell, leading to BZ effects that otherwise would complicate the analysis here. Note that although the breathing distortion is known to drive a MIT at the bulk level, we omit it here so we can estimate the band effective masses.

Figure 7 shows the Ni e_g orbital-resolved electronic band structure throughout the tetragonal BZ using the 'fat-bands' method[47], which allows us to distinguish the different orbital character of the Bloch states near the Fermi level. Consistent with the ionic picture of low-spin Ni^{3+}, the states at E_F are primarily of Ni d_{z^2} and $d_{x^2-y^2}$ symmetry with partial occupation of both spin channels. We find spin moments of 0.97 μ_B on the Ni sites in this configuration with a small amount of spin density located on the oxygen ligands because of itinerancy.

Classical approach in the two-band model. The key result from the DFT calculations given above (that should be quite robust, even in the presence of more complicated crystal distortions) is that there are multiple partially occupied bands with rather different effective masses. For example, consider the electron-like dispersion around the Γ point and the hole-like dispersion around the A point in Fig. 7. As was argued in a recent work by Maslov *et al.*[20], two more bands with different effective masses are key ingredients to stabilize NFL behaviour when

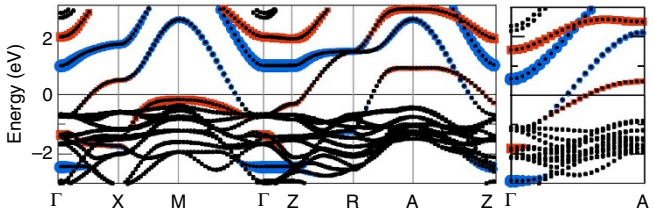

Figure 7 | Electronic band structure plot for $NdNiO_3$ along high-symmetry directions at ~0% strain. The orbital decomposed Ni d_{z^2} (red) and $d_{x^2-y^2}$ (blue) electronic structure for AFM $NdNiO_3$. The symbols' size correspond to the magnitude of the Bloch states projected onto each atomic orbital, and black bands close to the Fermi energy are predominantly of oxygen *p* character. (right) Low-energy electronic structure along the path from the zone centre to zone corner.

quantum critical fluctuations are also present in the heavier of the two bands. To motive this result, we first consider a minimal two-band model and then later generalize to multiple bands.

The classical equations of motion for two set of carries s,d are,

$$\frac{d}{dt}\mathbf{P}_s = -e_s\mathbf{E} - \frac{\mathbf{P}_s}{\tau_s} - \frac{m_d}{\tau_{sd}}\left(\frac{\mathbf{P}_s}{m_s} - \frac{\mathbf{P}_d}{m_d}\right), \quad (1)$$

$$\frac{d}{dt}\mathbf{P}_d = -e_d\mathbf{E} - \frac{\mathbf{P}_d}{\tau_d} - \frac{m_s}{\tau_{sd}}\left(\frac{\mathbf{P}_d}{m_d} - \frac{\mathbf{P}_s}{m_s}\right), \quad (2)$$

where $\mathbf{P}$ is momentum, e_s is the charge of s carriers, e_d the charge of the d carriers, m_s,m_d the respective masses of the carriers, $\mathbf{E}$ the applied electric field, τ_s and τ_d the respective scattering times of the carriers on impurities, and τ_{sd} the interband-scattering time. In these equations, the third term on the right-hand side accounts for the friction between carriers, whereas the first two terms are standard for a single-band model.

Solving these equations and taking the limit $t \to \infty$, we obtain the following expressions for the momenta. We also take $e_s = e_d = e$ for bands of like charge (two electrons, for example),

$$\mathbf{P}_s = -\frac{\frac{1}{\tau_d} + \frac{1}{\tau_{sd}}\left(1 + \frac{m_s}{m_d}\right)}{\frac{1}{\tau_s\tau_d} + \frac{1}{\tau_{sd}}\left(\frac{1}{\tau_s}\frac{m_s}{m_d} + \frac{1}{\tau_d}\frac{m_d}{m_s}\right)}\mathbf{E}, \quad (3)$$

$$\mathbf{P}_d = -\frac{\frac{1}{\tau_s} + \frac{1}{\tau_{sd}}\left(1 + \frac{m_d}{m_s}\right)}{\frac{1}{\tau_s\tau_d} + \frac{1}{\tau_{sd}}\left(\frac{1}{\tau_s}\frac{m_s}{m_d} + \frac{1}{\tau_d}\frac{m_d}{m_s}\right)}\mathbf{E}, \quad (4)$$

which leads to the conductivity for each carrier,

$$\sigma_s = \frac{n_s e^2}{m_s}\frac{\frac{1}{\tau_d} + \frac{1}{\tau_{sd}}\left(1 + \frac{m_s}{m_d}\right)}{\frac{1}{\tau_s\tau_d} + \frac{1}{\tau_{sd}}\left(\frac{1}{\tau_s}\frac{m_s}{m_d} + \frac{1}{\tau_d}\frac{m_d}{m_s}\right)}, \quad (5)$$

$$\sigma_d = \frac{n_d e^2}{m_d}\frac{\frac{1}{\tau_s} + \frac{1}{\tau_{sd}}\left(1 + \frac{m_d}{m_s}\right)}{\frac{1}{\tau_s\tau_d} + \frac{1}{\tau_{sd}}\left(\frac{1}{\tau_s}\frac{m_s}{m_d} + \frac{1}{\tau_d}\frac{m_d}{m_s}\right)}, \quad (6)$$

where $n_{s,d}$ is the electron density for each band. The total resistivity for two electron bands is

$$\rho_{ee} = (\sigma_s + \sigma_d)^{-1}. \quad (7)$$

If one further assumes 2D parabolic bands, the Fermi energy is described in terms of masses and electron density as

$$\varepsilon_F = \pi\hbar^2\frac{n_s}{m_s} = \pi\hbar^2\frac{n_d}{m_d}, \quad (8)$$

so that the total resistivity for two electron bands $\rho_{ee} = (\sigma_s + \sigma_d)^{-1}$ becomes

$$\rho_{ee} = \frac{\pi\hbar^2}{e^2\varepsilon_F}\frac{\frac{1}{\tau_s\tau_d} + \frac{1}{\tau_{sd}}\left(\frac{1}{\tau_s}\frac{m_s}{m_d} + \frac{1}{\tau_d}\frac{m_d}{m_s}\right)}{\frac{1}{\tau_s} + \frac{1}{\tau_d} + \frac{1}{\tau_{sd}}\left(2 + \frac{m_s}{m_d} + \frac{m_d}{m_s}\right)}. \quad (9)$$

This relation is identical to equation (6) in ref. 20. Moreover, in 3D, or for non-parabolic bands, the numerator is modified as the relation in equation (8) no longer holds. The key feature of equation (9) is that the dominant temperature dependence of ρ_{ee} enters through τ_{sd} as the impurity scattering times τ_s, τ_d are only weakly temperature dependent and can be taken as a constant to a good approximation when quantum criticality is present[20].

The key result here is that for a window of temperatures in 2D $\tau_{sd} \propto T^{-4/3}$ with $\mathbf{q} = 0$ critical fluctuations, whereas for 3D, $\tau_{sd} \propto T^{-5/3}$. This temperature dependence leads to $\rho_{ee} \propto T^{4/3}$ in 2D and $\rho_{ee} \propto T^{5/3}$ in 3D (ref. 20), which are the exponents we measure in our experiments. Moreover, a more detailed calculation shows (see following sections) that ignoring the 'vertex corrections' at higher temperatures will lead to $\rho_{ee} \propto T$ in 3D, also in excellent agreement with our experimental results.

Three-band model. The equation of motion is generalized to a multiple band model (here we consider three) with their own masses, relaxations and interband scatterings:

$$\frac{d}{dt}\mathbf{P}_i = -e_i\mathbf{E} - \frac{\mathbf{P}_i}{\tau_i} - \sum_{j\neq i}\frac{m_j}{\tau_{ij}}\left(\frac{\mathbf{P}_i}{m_i} - \frac{\mathbf{P}_j}{m_j}\right). \tag{10}$$

Here we assume that all three bands are of electron type, but with different masses. Specifically, we assume one of the bands is very massive, that is, $m_3 \gg m_1, m_2$, implying $\tau_3 \ll \tau_1, \tau_2$. We assume that band 3 is close to criticality, whereas the bands 1 and 2 are off criticality. To make things simpler, we also assume that the scattering between bands 1 and 2 is not effective, that is, $\tau_{12}\to\infty$, which is consistent with these bands being off criticality. We also take $\tau_{13}=\tau_{23}=\tau$. Performing the same steps as above, we arrive at

$$\sigma(T) = \frac{e^2\varepsilon_F}{\pi\hbar^2}\frac{\tau_1+\tau_2}{m_1\tau_2+m_2\tau_1}\frac{m_1m_2}{m_3}\tau, \tag{11}$$

$$\rho(T) = \frac{\pi\hbar^2}{e^2\varepsilon_F}\frac{m_1\tau_2+m_2\tau_1}{\tau_1+\tau_2}\frac{m_3}{m_1m_2}\frac{1}{\tau}. \tag{12}$$

The temperatures setting the upper and lower limits of the NFL behaviours $\rho(T)\propto T^{4/3}$ in 2D and $\rho(T)\propto T^{5/3}$ in 3D are determined from[20]

$$\frac{1}{\tau(T_1')}\left(\frac{\tau_3}{\tau_1}\frac{m_3}{m_2}+\frac{\tau_3}{\tau_2}\frac{m_3}{m_1}+\frac{m_3}{m_2}+\frac{m_3}{m_1}\right)\frac{\tau_1\tau_2}{\tau_1+\tau_2} = 1 \Rightarrow \tag{13}$$

$$\frac{1}{\tau(T_1')} = \frac{1}{\tau_3}\frac{1}{m_3}\frac{\tau_1+\tau_2}{\frac{\tau_1}{m_1}+\frac{\tau_2}{m_2}+\frac{\tau_1\tau_2}{\tau_3}\left(\frac{1}{m_1}+\frac{1}{m_2}\right)},$$

$$\frac{1}{\tau(T_2')}\left(\tau_2\frac{m_3}{m_2}+\tau_1\frac{m_3}{m_1}\right) = 1 \Rightarrow \frac{1}{\tau(T_2')} = \frac{1}{\frac{\tau_1}{m_1}+\frac{\tau_2}{m_2}}\frac{1}{m_3}, \tag{14}$$

which implies that

$$\frac{\tau(T_2')}{\tau(T_1')} \gg 1 \Rightarrow T_1' \gg T_2'. \tag{15}$$

Thus, the scaling regime is $T_2' \ll T \ll T_1'$, where the resistivity goes as $\rho(T)\propto\frac{1}{\tau(T)}$.

We are interested in knowing how the temperature window of scaling is extended or contracted as the number of bands are increased. To compare with a two-band model, we reduce the definitions of characteristic temperatures in equation (13 and 14) to a two-band model by simply dropping band 2. We have,

$$\frac{1}{\tau(T_1)} = \frac{1}{\tau_3}\frac{m_1}{m_3}, \tag{16}$$

$$\frac{1}{\tau(T_2)} = \frac{1}{\tau_1}\frac{m_1}{m_3}. \tag{17}$$

Hence, we conclude this window extends as

$$T_2' < T_2 \ll T \ll T_1' < T_1. \tag{18}$$

Therefore, we can see that as the number of bands increase the lower and upper limits of the window is pushed down to lower temperatures. This is seen in Fig. 8.

Boltzmann equations in the presence of impurities. We consider the interband scattering via interactions between electrons mediated with critical fluctuations. This was carried out in ref. 20. The corresponding coupled Boltzmann equations are,

$$e\mathbf{v}_i(\mathbf{k}_i)\cdot\mathbf{E}n_i' = -\sum_{j\neq i} I_{ee}^{ij}[f_i,f_j] - \frac{f_i(\mathbf{k}_i)-n_i}{\tau_i}, \tag{19}$$

where n is the undisturbed Fermi distribution, whereas f is the disturbed one. We also used the relaxation time approximation (relaxation time τ_i) to include the scattering off impurities. I_{ee}^{ij} is the collision integral describing scattering of electrons of the ith band from jth band, and is expressed as,

$$I_{ee}^{ij}[f_i,f_j] = \int\frac{d^2\mathbf{k}_j}{(2\pi)^2}\int\frac{d^2\mathbf{k}'_i}{(2\pi)^2}\int\frac{d^2\mathbf{k}'_j}{(2\pi)^2}W(\mathbf{q},\omega)[f_i(\mathbf{k}_i)f_j(\mathbf{k}_j)(1-f_i(\mathbf{k}'_i))$$

$$\times(1-f_j(\mathbf{k}'_j)) - f_i(\mathbf{k}'_i)f_j(\mathbf{k}'_j)(1-f_i(\mathbf{k}'_i))\,(1-f_j(\mathbf{k}'_j))]$$

$$\times\,\delta(\varepsilon_{\mathbf{k}_i}+\varepsilon_{\mathbf{k}_j}-\varepsilon_{\mathbf{k}'_i}-\varepsilon_{\mathbf{k}'_i})\,\delta(\mathbf{k}_i+\mathbf{k}_j-\mathbf{k}'_i-\mathbf{k}'_j) \tag{20}$$

where $W(\mathbf{q},\omega)$ is the interaction matrix and $f(\mathbf{k})$ is Fermi distribution function. Solving the Boltzmann equations, we obtain the following relation for the resistivity of the system,

$$\rho_{ee} = \frac{\pi\hbar^2}{e^2\varepsilon_F}\frac{\frac{1}{\tau_s\tau_d}+\frac{1}{\tau_{sd}}\left(\frac{1}{\tau_s}\frac{m_s}{m_d}+\frac{1}{\tau_d}\frac{m_d}{m_s}\right)}{\frac{1}{\tau_s}+\frac{1}{\tau_d}+\frac{1}{\tau_{sd}}\left(2+\frac{m_s}{m_d}+\frac{m_d}{m_s}\right)}, \tag{21}$$

where

$$\frac{1}{\tau_{sd}} = \frac{1}{2T}\frac{\sqrt{m_sm_d}}{\varepsilon_F^2}\int\frac{d\omega}{2\pi}\int\frac{dq}{2\pi}qW(q,\omega)\omega^2N(\omega)(N(\omega)+1), \tag{22}$$

with $N(\omega)$ the usual boson distribution function.

The bare interaction between s and d electrons V_{sd}^0 is mediated by fluctuations,

$$V_{sd}(q,\omega) = \frac{V_{sd}^0}{1-\chi_{dd}(q,\omega)V_{dd}^0}. \tag{23}$$

Expanding $\chi_{dd}(q,\omega)$,

$$\chi_{dd}(q,\omega) \simeq \chi_0 + cq^2 - ib\frac{\omega}{q}, \tag{24}$$

we can see that the if $V_{dd}^0\chi_0 \to 1$, the criticality would be associated with dynamical exponent $z=3$. Let us define

$$\chi(q,\omega) = \frac{1}{cq^2-ib\frac{\omega}{q}}, \tag{25}$$

then we can write the scattering matrix as

$$W(q,\omega) = |V_{sd}|^2 = \left(\frac{V_{sd}^0}{V_{dd}^0}\right)^2\frac{1}{b}\frac{q}{\omega}\mathrm{Im}\chi(q,\omega). \tag{26}$$

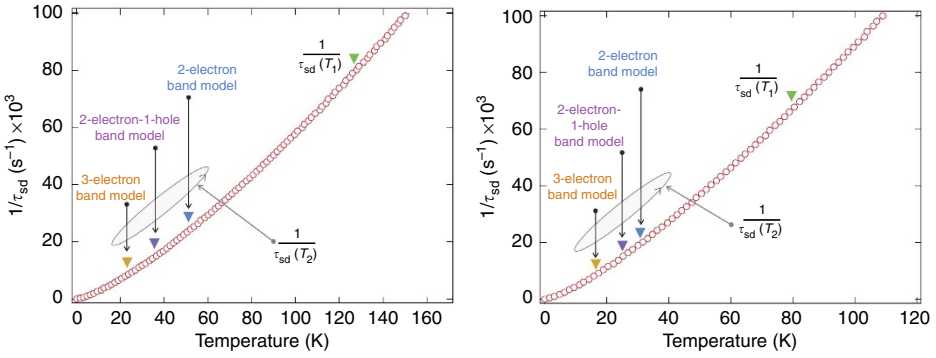

Figure 8 | Interband scattering rate. Left: interband scattering rate (s^{-1}) in equation (27) versus temperature (in K). T_1 and T_2 stand for upper and lower part of scaling regime, where relations in equation (30) and equation (31) are satisfied. The plot is obtained for $b=c=1$. Models with different number of bands lead to shifting of scaling regime. Downward arrows: green arrow denotes upper limit of scaling regime that does not change so much with increasing bands but is suppressed slightly. Above the temperature T_1, the resistivity is expected to crossover to $T\ln T$ (see equation (29) and discussion immediately below it), consistent with experiment. Blue, purple and brown arrows stand for lower part of scaling regime that are shifted to lower temperature with increasing bands and taking hole-like states as well into account. Right: same as left but with different set of parameters: $c=0.28$ and $b=5.8$.

This allows one to write the scattering rate as

$$\frac{1}{\tau_{\rm sd}}=\frac{1}{2T}\frac{\sqrt{m_s m_d}}{\varepsilon_{\rm F}^2}\left(\frac{V_{sd}^0}{V_{dd}^0}\right)^2\frac{1}{b}\int\frac{d\omega}{2\pi}\int\frac{dq}{2\pi}q\frac{\omega}{q}{\rm Im}\chi(q,\omega)N(\omega)(N(\omega)+1)\underbrace{q^2}. \tag{27}$$

This relation is identical to the relation for scattering rate close to a FM phase transition[48]. Moreover, the term in braces comes from the vertex corrections to render the conductivity finite. The temperature scaling goes as,

$$\begin{array}{l}\frac{1}{\tau_{\rm sd}}\propto T^{4/3}\text{in 2D}\\ \frac{1}{\tau_{\rm sd}}\propto T^{5/3}\text{in 3D}\end{array} \tag{28}$$

with vertex corrections, and

$$\begin{array}{l}\frac{1}{\tau_{\rm sd}}\propto T^{2/3}\text{in 2D}\\ \frac{1}{\tau_{\rm sd}}\propto T\ln T\text{ in 3D}\end{array} \tag{29}$$

without vertex corrections. Generally, arguments suggest[49] that vertex corrections can often be ignored at higher temperatures, which we assume is set by the temperature T' in our experiments. Thus, equation (28) applies at temperatures below T', and equation (29) at temperatures above T'.

If we compare the results above with the exponents measured in our experiments, it is tempting to interpret the transport below T' as quasi-2D for $\varepsilon=-0.3$ and -1.2% and quasi-3D for $\varepsilon=-2.9\%$. On the basis of the rather general results (mechanism independent), equation (28) and equation (29), it also appears the transport is quasi-3D above T'. For a $NdNiO_3$ to change from effectively 2D to effectively 3D under increasing compressive strain is not unexpected[21]. However, one should check that an estimate of the temperature T' is in rough agreement with the experimentally determined value.

Temperature dependence of transport scattering rate. From above, one could see that the NFL scaling (with the vertex correction) is achieved within a temperature window; see equation (18). Here we give a rough estimate of the scaling of this window with the number of bands and rough estimates for experimental parameters. A precise determination of the scaling region requires detailed knowledge of the band structure of the model and the exact mechanism of the quantum criticality. We present a simplified case here and consider parabolic bands (although the DFT results predict rather non-trivial Fermi surface shapes). The shape and topology of the different Fermi surfaces will numerically affect the result but the order of magnitude effects can be determined within this approximation.

Here we use the experimental values for electrical resistivity in the temperature range corresponding to NFL with temperature scaling $T^{4/3}$ to determine what temperature window they predict according to following formulas derived for the three-band model,

$$\begin{array}{l}\frac{1}{\tau(T_1)}=\frac{1}{\tau_3}\frac{m_1}{m_3},\\ \frac{1}{\tau(T_2)|}=\frac{1}{\tau_1}\frac{m_1}{m_3},\end{array} \tag{30}$$

which can be reduced to the two-band model s–d model as derived in ref. 20,

$$\begin{array}{l}\frac{1}{\tau_{\rm sd}(T_1)}=\frac{1}{\tau_{\rm s}}\frac{m_{\rm s}}{m_{\rm d}},\\ \frac{1}{\tau_{\rm sd}(T_2)}=\frac{1}{\tau_{\rm d}}\frac{m_{\rm s}}{m_{\rm d}}.\end{array} \tag{31}$$

Our goal is to see whether this approach can yield results in semiquantitative agreement with experiment. (We find it does in good accord.) We use some typical values for the parametrized susceptibility in equation (25): $c=b=1$ and choose that the interband interaction to be very small $\frac{V_{\rm sd}^0}{V_{\rm dd}^0}\sim 10^{-3}$. We numerically calculate equation (27) as shown in Fig. 8.

For a two-band model, the upper and lower parts of the $T^{4/3}$ temperature window are exhibited by downward green and blue arrows, respectively. As we showed in the three-band model, the lower part of window can be pushed down to lower temperatures as the number of bands increases. For example, for the three-electron band model, it is clear to see that the lower bound is decreased by almost a factor of 2, whereas the upper bound changes very little. According to our DFT calculations, actual band structure of the system is complex, and exhibits open Fermi surfaces. Perhaps, if these details are taken into account, the lower bound of temperature window will go down even further to the lowest measured temperature.

We also considered another set of parameters ($c=0.28$ and $b=5.8$), and the corresponding plot is shown in Fig. 8. Although the scaling window shifts to slightly lower temperatures, it still remains within a physical range of temperatures, which are not too far away from the experimental values. This indicates that despite the simplifications mentioned above, the model appears to capture the most important underlying physics.

Possible mechanisms of criticality. In the following, we speculate on two possible mechanisms that (in principle) could lead to the exotic scaling behaviour observed in our experiment.

There is a paramagnetic insulator phase in the phase diagram shown in Fig. 2. This phase is close to a charge disproportionate state with two inequivalent Ni sites[50]. Although magnetic circular dichroism on Ni L-edge measurement exhibits the existence of local magnetism with short-range correlations, which brings the idea of a SL phase into consideration, we assume that charge disproportionation is a largely relevant description of this phase. More specifically, it would be natural to assume that the NFL phase in proximity to the charge-ordered phase inherits some signatures of density fluctuations. Thus, we can assume that on the compressive side the charge density is almost uniform with the presence of long wavelength density fluctuations in it. Then, as the compressive strain decreases, the density fluctuations act to give rise to charge ordering on tensile side. Moreover, it seems that the role of oxygen ions is critically important here because of the relevant charge transfer p–d physics in the insulating phase.

In the past, phase separation and associated density fluctuations have been proposed as a possible mechanism for anomalous normal state behaviour of cuprates, as such fluctuations can induce large scattering amplitude among quasiparticles[51,52]. Both weak[53] and strong[54] coupling limits of the on-site Hubbard interactions indicate the occurrence of a charge instability driven by intersite interactions between transition ions and oxygens.

A mean-field treatment of the problem shows a transition from a metallic phase to insulating phase. Near the phase transition, the density fluctuations give rise to a massless mode. Here the total charge density n_d+n_p and charge transfer density n_d-n_p are strongly fluctuating. These zero modes substantially modify the effective scattering amplitude between quasiparticles via the vertex interaction with bosonic degrees of freedom. These latter modes come from the fluctuations of the fields coupling to the mean-field parameters. The corresponding propagators can be described as follows,

$$D(q,{\rm w})=N^{-1}[2B+\Pi(q,{\rm w})]^{-1}, \tag{32}$$

where N is the number of fermion flavours in a $1/N$ expansion, $\Pi(q,\omega)$ is the polarization including vertex interactions and B describes the spectrum of bosons. The effective interaction between quasiparticles is then given by

$$\Gamma_{kk'}(q,{\rm w})=-\Lambda(k',-q)D(q,{\rm w})\Lambda(k,q), \tag{33}$$

where Λ stands for vertex interaction.

The charge instability is given by the diverging of the density–density correlation function leading to

$$\det(2B+\Pi)=0, \tag{34}$$

that immediately gives rise to a diverging effective interaction. One can show that the spectral density of the total density–density correlation function exhibits a peak at small momentum transfers, that is, $\mathbf{q}\approx 0$ instability. This mode is damped into the particle-hole continuum, which in turn modifies the self-energy of the quasiparticles thus taking it away from the conventional Fermi liquid behaviour.

Phonons are also a possible driving force to induce the charge instability in the system. The phonons are coupled to charge density at both transition ions and oxygen sites[55]. The charge instability will always take place by increasing the large bare charge-transfer difference $(\varepsilon_{\rm p}-\varepsilon_{\rm d})/t_{\rm pd}$, where $\varepsilon_{\rm p(d)}$ is the on-site energy and $t_{\rm pd}$ is the transition ion-oxygen hopping. This latter can be easily tuned in our system via the compressive strain. Near the phase separation instability, the anomalous scattering amplitude is identified to be of the following form[52,56]

$$\Gamma(q,\omega)\sim-\frac{1}{Bq^2-iC\frac{\omega}{q}+D}, \tag{35}$$

where $D=D(\delta-\delta_{\rm c})$ measures the closeness to criticality via doping. As clearly seen, this effective interaction is singular with dynamical exponent $z=3$, which in turn strongly modifies the scattering relaxation and transport rates; the singular interaction thus make them to have NFL character. In both cases above, an enlarged unit cell would naturally lead to $\mathbf{q}$ wavevector fluctuations.

References

1. Imada, M., Fujimori, A. & Tokura, Y. Metal-insulator transitions. *Rev. Mod. Phys.* **70,** 1039–1263 (1998).
2. Zaanen, J., Sawatzky, G. A. & Allen, J. W. Band gaps and electronic structure of transition-metal compounds. *Phys. Rev. Lett.* **55,** 418–421 (1985).
3. Chakhalian, J., Millis, A. J. & Rondinelli, J. Whither the oxide interface. *Nat. Mater.* **11,** 92–94 (2012).
4. Mannhart, J. & Schlom, D. G. Oxide interfaces ł An opportunity for electronics. *Science* **327,** 1607–1611 (2010).
5. Catalan, G. Progress in perovskite nickelate research. *Phase Transit.* **81,** 729–749 (2008).
6. Medarde, M. L. Structural, magnetic and electronic properties of $RNiO_3$ perovskites (R = rare earth). *J. Phys. Condens. Matter* **9,** 1679–1707 (1997).
7. Mizokawa, T. *et al.* Origin of the band gap in the negative charge-transfer-energy compound $NaCuO_2$. *Phys. Rev. Lett.* **67,** 1638–1641 (1991).
8. Sarma, D. D. Electronic structure of transition metal compounds: photoemission experiments and model Hamiltonian calculations. *J. Solid State Chem.* **88,** 45–52 (1990).
9. Khomskii, D. I. Unusual valence, negative charge-transfer gaps and self-doping in transition-metal compound. *Lith. Phys. J.* **37,** 65–72 (1997).
10. Mizokawa, T., Khomskii, D. I. & Sawatzky, G. A. Spin and charge ordering in self-doped Mott insulators. *Phys. Rev. B* **61,** 11263–11266 (2000).

11. Alonso, J. A. *et al.* Charge disproportionation in $RNiO_3$ perovskites: simultaneous metal-insulator and structural transition in $YNiO_3$. *Phys. Rev. Lett.* **82,** 3871–3874 (1999).
12. Staub, U. *et al.* Direct observation of charge order in an epitaxial $NdNiO_3$ film. *Phys. Rev. Lett.* **88,** 126402 (2002).
13. Goodenough, J. B. Covalent exchange vs superexchange in two nickel oxides. *J. Solid State Chem.* **127,** 126–127 (1996).
14. Jian, L. *et al.* Strain-mediated metal-insulator transition in epitaxial ultrathin films of $NdNiO_3$. *Appl. Phys. Lett.* **96,** 233110 (2010).
15. Zhou, J.-S., Goodenough, J. B. & Dabrowski, B. Pressure-induced non-Fermi liquid behavior of $PrNiO_3$. *Phys. Rev. Lett.* **94,** 226602 (2005).
16. Möbius, A. Comment on metal-insulator transition in amorphous $Si_{1-x}Cr_x$. *Solid State Comm.* **73,** 215–219 (1990).
17. Balents, L. Spin liquids in frustrated magnets. *Nature* **464,** 199–208 (2010).
18. Suter, A. *et al.* Two-dimensional magnetic and superconducting phases in metal-insulator $La_{2-x}Sr_xCuO_4$ superlattices measured by muon-spin rotation. *Phys. Rev. Lett.* **106,** 237003 (2011).
19. Rajeev, K. P., Shivashankar, G. V. & Raychaudhuri, A. K. Low-temperature electronic properties of a normal conducting perovskite oxide ($LaNiO_3$). *Solid State Commun.* **79,** 591–595 (1991).
20. Maslov, D. L., Yudson, V. I. & Chubukov, A. V. Resistivity of a non-Galilean invariant fermi liquid near Pomeranchuk quantum criticality. *Phys. Rev. Lett.* **106,** 106403 (2011).
21. Angel, R. J., Zhao, J. & Ross, N. L. General rules for predicting phase transitions in perovskites due to octahedral tilting. *Phys. Rev. Lett.* **95,** 025503 (2005).
22. Blasco, J. & Garcia, J. A comparative study of the crystallographic, magnetic and electrical properties of the $Nd_{1-x}La_xNiO_{3-\delta}$ system. *J. Phys. Condens. Matter* **6,** 10759–10772 (1994).
23. Julian, S. R. *et al.* Non-Fermi-liquid behaviour in magnetic d- and f-electron systems. *J. Magn. Magn. Mater.* **177,** 265–270 (1998).
24. Moriya, T. & Takimoto, T. Anomalous properties around magnetic instability in heavy electron systems. *J. Phys. Soc. Jpn* **64,** 960–969 (1995).
25. Sarma, D. D., Shanthi, N. & Mahadevan, P. Electronic excitation spectra from ab initio band-structure results for $LaMO_3$ (M = Cr,Mn,Fe,Co,Ni). *Phys. Rev. B* **54,** 1622–1637 (1996).
26. Medarde, M. *et al.* $RNiO_3$ perovskites (R = Pr,Nd): Nickel valence and the metal-insulator transition investigated by x-ray-absorption spectroscopy. *Phys. Rev. B* **46,** 14975–14984 (1992).
27. Merz, M. *et al.* Site-specific X-ray absorption spectroscopy of $Y_{1-x}Ca_xBa_2Cu_3O_{7-y}$: overdoping and role of apical oxygen for high temperature superconductivity. *Phys. Rev. Lett.* **80,** 5192–5195 (1998).
28. Ohta, Y., Tohyama, T. & Maekawa, S. Charge-transfer gap and superexchange interaction in insulating cuprates. *Phys. Rev. Lett.* **66,** 1228–1231 (1991).
29. Zaanen, J. & Sawatzky, G. A. Systematics in band gaps and optical spectra of 3D transition metal compounds. *J. Solid State Chem.* **88,** 8–27 (1990).
30. Bodenthin, Y. *et al.* Magnetic and electronic properties of $RNiO_3$ (R = Pr, Nd, Eu, Ho and Y) perovskites studied by resonant soft X-ray magnetic powder diffraction. *J. Phys. Condens. Matter.* **23,** 036002 (2011).
31. Doering, D. *et al.* Development of a compact fast CCD camera and resonant soft X-ray scattering endstation for time-resolved pump-probe experiments. *Rev. Sci. Instrum.* **82,** 073303 (2011).
32. Zhou, J.-S., Goodenough, J. B. & Dabrowski, B. Transition from Curie-Weiss to enhanced Pauli paramagnetism in $RNiO_3$ (R = La,Pr,Gd). *Phys. Rev. B* **67,** 020404 R (2003).
33. Alonso, J. A. *et al.* High-temperature structural evolution of $RNiO_3$ (R = Ho;Y; Er; Lu) perovskites: charge disproportionation and electronic localization. *Phys. Rev. B* **64,** 094102 (2001).
34. Medarde, M., Lacorre, P., Conder, K., Fauth, F. & Furrer, A. Giant ^{16}O–^{18}O isotope effect on the metal-insulator transition of $RNiO_3$ perovskites (R = rare earth). *Phys. Rev. Lett.* **80,** 2397–2400 (1998).
35. Zhou, J.-S., Goodenough, J. B., Dabrowski, B., Klamut, P. W. & Bukowski, Z. Probing the metal-insulator transition in Ni(III)-oxide perovskites. *Phys. Rev. B* **61,** 4401–4404 (2000).
36. Mazin, I. *et al.* Charge ordering as alternative to Jahn-Teller distortion. *Phys. Rev. Lett.* **98,** 176406–176409 (2007).
37. Escote, M. T., Barbeta, V. B., Jardim, R. F. & Campo, J. Metal-insulator transition in $Nd_{1-x}Eu_xNiO_3$ compounds. *J. Phys. Condens. Matter.* **18,** 6117–6132 (2006).
38. Cheng, J.-G., Zhou, J.-S., Goodenough, J. B., Alonso, J. A. & Martinez-Lope, M. J. Pressure dependence of metal-insulator transition in perovskites $RNiO_3$ (R = Eu, Y, Lu). *Phys. Rev. B* **82,** 085107 (2010).
39. Lee, P. A. & Ramakrishnan, T. V. Disordered electronic systems. *Rev. Mod. Phys.* **57,** 287–337 (1985).
40. Blochl, P. E. Projector augmented-wave method. *Phys. Rev. B* **50,** 17953–17979 (1994).
41. Kresse, G. & Furthmller, J. Efficiency of ab-initio total energy calculations for metals and semiconductors using a plane-wave basis set. *Comput. Mater. Sci.* **6,** 15–50 (1996).
42. Kresse, G. & Joubert, D. From ultrasoft pseudopotentials to the projector augmented-wave method. *Phys. Rev. B* **59,** 1758–1775 (1999).
43. Perdew, J. P., Burke, K. & Ernzerhof, M. Generalized gradient approximation made simple. *Phys. Rev. Lett.* **77,** 3865–3868 (1996).
44. Anisimov, V. I., Aryasetiawan, F. & Lichtenstein, A. I. First-principles calculations of the electronic structure and spectra of strongly correlated systems: the LDA + U method. *J. Phys. Condens. Matter* **9,** 767–808 (1997).
45. Dudarev, S. L., Botton, G. A., Savrasov, S. Y., Humphreys, C. J. & Sutton, A. P. Electron-energy-loss spectra and the structural stability of nickel oxide: an LSDA + U study. *Phys. Rev. B* **57,** 1505–1509 (1998).
46. Prosandeev, S., Bellaiche, L. & Iniguez, J. Ab initio study of the factors affecting the ground state of rare-earth nickelates. *Phys. Rev. B* **85,** 214431 (2012).
47. Jepsen & Andersen, O. Calculated electronic structure of the sandwich d1 metals LaI_2 and CeI_2: application of new LMTO techniques. *Zeitschrift Phys.* **97,** 35–47 (1995).
48. Smith, R. P. *et al.* Marginal breakdown of the Fermi-liquid state on the border of metallic ferromagnetism. *Nature* **455,** 1220–1223 (2008).
49. Mahan, G. *Many-Particle Physics* (Kluwer Academic/Plenum Publishers), 2000.
50. Chakhalian, J. *et al.* Asymmetric orbital-lattice interactions in ultrathin correlated oxide films. *Phys. Rev. Lett.* **107,** 116805 (2011).
51. Emery, V. & Kivelson, S. Frustrated electronic phase separation and high-temperature superconductors. *Phys. C Superconductivity* **209,** 597–621 (1993).
52. Castellani, C., Di Castro, C. & Grilli, M. Singular quasiparticle scattering in the proximity of charge instabilities. *Phys. Rev. Lett.* **75,** 4650–4653 (1995).
53. Bang, Y., Kotliar, G., Castellani, C., Grilli, M. & Raimondi, R. Phase separation, charge-transfer instability, and superconductivity in the three-band extended hubbard model: Weak-coupling theory. *Phys. Rev. B* **43,** 13724–13727 (1991).
54. Raimondi, R., Castellani, C., Grilli, M., Bang, Y. & Kotliar, G. Charge collective modes and dynamic pairing in the three-band Hubbard model. II. Strong-coupling limit. *Phys. Rev. B* **47,** 3331–3346 (1993).
55. Grilli, M. & Castellani, C. Electron-phonon interactions in the presence of strong correlations. *Phys. Rev. B* **50,** 16880–16898 (1994).
56. Becca, F., Tarquini, M., Grilli, M. & Di Castro, C. Charge-density waves and superconductivity as an alternative to phase separation in the infinite-U Hubbard-Holstein model. *Phys. Rev. B* **54,** 12443–12457 (1996).
57. Data-Sheets http://www.crystec.de/datasheets-e.html (2013).
58. Uecker, R. *et al.* Growth conditions and composition of SrPrGaO4 single crystals. *J. Cryst. Growth* **174,** 320–323 (1997).

Acknowledgements

We acknowledge numerous insightful discussions with D.I. Khomskii, A.J. Millis, D.D. Sarma, S. Okamoto, G.A. Sawatzky, S. Papanikolaou, D. Maslov and M. Lawler. We also acknowledge B.Dabrowski for providing the bulk reference powders. J.C. was supported by DOD-ARO under the Grant number 0402-17291 and NSF Grant number DMR-0747808, M.K. and G.A.F. by DOD-ARO Grant number W911NF-09-1-0527, W911NF-12-1-0573, DARPA D13AP00052 and NSF Grant number DMR-0955778. J.M.R. was supported by DARPA under Award number N66001-12-1-4224. J.L. acknowledges the support from the ALS Doctoral Fellowship programme. The density functional studies made use of the CARBON cluster at the Center for Nanoscale Materials (Argonne National Laboratory) supported by the US DOE, Office of Science, BES, under Contract number DE-AC02-06CH11357. Work at ALS is supported by the Director, Office of Science, Office of Basic Energy Sciences, of the US Department of Energy under Contract number DE-AC02-05CH11231. Work at the APS is supported by the US Department of Energy, Office of Science under Grant number DE-AC02-06CH11357.

Author contributions

J.L. and J.C. conceived and designed the experiments. Samples were prepared and characterized by M.Kareev, J.L., B.G. and P.J.R. J.L. and B.G. performed resistivity measurements. J.L., B.G. and J.W.F. carried out the XAS data collection. J.L., Y.-D.C., A.C., N.T. and J.G. participated in the resonant X-ray scattering experiments. J.L., J.W.F. and J.C. carried out data analysis. M.Kargarian and G.A.F. were responsible for the analytical calculations for the transport theory and provided theoretical inputs to the quantum critical behaviour. The density functional theory calculations were performed by J.M.R. Y.D.C., J.G., J.M.R. and J.W.F. helped revise the manuscript. J.L., M.Kargarian, G.A.F. and J.C. co-wrote the paper.

Additional information

Competing financial interests: The authors declare no competing financial interests.

How to cite this article: Liu, J. *et al.* Heterointerface engineered electronic and magnetic phases of $NdNiO_3$ thin films. *Nat. Commun.* 4:2714 doi: 10.1038/ncomms3714 (2013).